

Detecting Anemia from Retinal Fundus Images

Akinori Mitani, MD, PhD¹

Yun Liu, PhD¹

Abigail Huang, MD¹

Greg S. Corrado, PhD¹

Lily Peng, MD, PhD¹

Dale R. Webster, PhD¹

Naama Hammel, MD¹

Avinash V. Varadarajan, MS¹

¹ Google AI Healthcare, Google, Mountain View, CA, USA

Corresponding author:

Akinori Mitani, MD, PhD

Google AI Healthcare

1600 Amphitheatre Parkway

Mountain View, CA 94043

amitani@google.com

Abstract	3
Introduction	4
Results	5
Discussion	8
Methods	11
Study participants	11
Definitions of anemia	12
Categories of predictive models	12
Development of the deep learning algorithms	13
Evaluating the algorithms	14
Ablation analysis	14
Code availability	15
Data availability	15
References	16
Acknowledgements	20
Author contributions	20
Competing interests	20
Tables and figures	21
Table 1. Basic characteristics of the development datasets and the validation dataset.	21
Table 2. Sensitivity at various levels of specificity.	23
Table 3. Accuracy of different methods to measure hemoglobin concentration.	24
Figure 1. Prediction of hemoglobin concentration, hematocrit and red blood cell count.	25
Figure 2. Correlation between residual errors of the combined model from multiple visits.	26
Figure 3. Prediction of anemia classifications.	27
Figure 4. Effects of masking parts of the image on the prediction of anemia and moderate anemia.	28
Figure 5. Effects of removing high-frequency information using Gaussian blur on the prediction of anemia and moderate anemia.	29
Supplementary information	30
Supplementary methods	30
Table S1. Prediction of complete blood count components.	31

Abstract

Despite its high prevalence, anemia is often undetected due to the invasiveness and cost of screening and diagnostic tests. Though some non-invasive approaches have been developed, they are less accurate than invasive methods, resulting in an unmet need for more accurate non-invasive methods. Here, we show that deep learning-based algorithms can detect anemia and quantify several related blood measurements using retinal fundus images both in isolation and in combination with basic metadata such as patient demographics. On a validation dataset of 11,388 patients from the UK Biobank, our algorithms achieved a mean absolute error of 0.63 g/dL (95% confidence interval (CI) 0.62-0.64) in quantifying hemoglobin concentration and an area under receiver operating characteristic curve (AUC) of 0.88 (95% CI 0.86-0.89) in detecting anemia. This work shows the potential of automated non-invasive anemia screening based on fundus images, particularly in diabetic patients, who may have regular retinal imaging and are at increased risk of further morbidity and mortality from anemia.

Introduction

Anemia is a public health problem affecting an estimated 1.62 billion people¹. In 2011, 29% of non-pregnant women worldwide were affected by anemia². As a major contributor to global burden of disease, anemia has far-reaching consequences for work and productivity and quality of life^{1,3,4}. As anemia is usually correctable⁵, timely detection and intervention are key. The most reliable indicator of anemia is hemoglobin concentration (Hb)¹, which is traditionally measured using a venous or capillary blood sample. However, these procedures are invasive and painful, can cause infection of patients and healthcare workers, and generate biohazardous waste⁶. Thus, there is a clear need for a non-invasive procedure.

Several non-invasive methods of estimating Hb are now available. Traditionally, subjective assessment of pallor of the conjunctiva, nail beds, tongue, and palms have been used as clinical signs indicating the presence of severe anemia, with a wide range of estimated sensitivities and specificities^{7,8}. Recently, it was reported that Hb can be estimated with high accuracy using automated algorithms from the color of fingernail beds in digital photographs taken by smartphones⁹. However, the algorithms were based on manually selected regions of interest on the fingernails, and their robustness and real-world performance remains to be assessed. Another two methods, occlusion spectroscopy and pulse-co-oximetry, use spectrophotometric sensors that non-invasively assess Hb by measuring light transmission through the tissue^{10,11}. These non-invasive methods are less accurate than the gold standard of venous blood laboratory analysis¹² and represent trade-offs between invasiveness, time, cost, and accuracy⁹.

Interestingly, anemia of sufficient severity has been known to manifest characteristic signs in the fundus of the eye¹³, and 20% of anemia patients have reported to develop extravascular lesions, with severity of anemia related to venous tortuosity¹⁴. Retinopathy is

observed in 28.3% of patients with anemia and/or thrombocytopenia, and low Hb level was associated with the presence of retinopathy¹⁴. However, the low prevalence of retinopathy among anemic patients limits its potential sensitivity as a stand-alone diagnostic feature, and fundus photographs have not been used to either detect anemia or quantify more precise Hb levels.

In this work, we explore the hypothesis that Hb can be quantified using noninvasive fundus photographs and deep learning (DL). DL has been previously shown to be highly effective in extracting information from images¹⁵. In ophthalmology, DL algorithms can detect eye conditions such as diabetic retinopathy, age-related macular degeneration, and glaucoma with accuracy comparable to human experts¹⁶⁻²¹. Additionally, some previously-unknown information can be extracted from fundus images, such as refractive error²², age, sex, and cardiovascular risk²³. Extending this, we show that DL can be leveraged to quantify Hb and detect anemia.

Results

This study was conducted using data from UK Biobank²⁴. In total, 114,205 fundus images from 57,163 patients were included in this study. In the validation set, the median age of the patients was 57.9 (50.0-63.8, interquartile range) years, 54.9% were female, and 91.1% were White (Table 1). Among all the patients, 3.7% had anemia, with Hb ranging from 6.4 [g/dL] to 19.6 [g/dL]. Additional patient demographics are summarized in Table 1.

Results of many blood tests including Hb are correlated with patients' metadata such as demographics. Some of these metadata, such as age and gender have previously been shown to be predictable using fundus images²³. Therefore to later ensure that our predictors were not solely predicting Hb measurements via age and gender, we first developed baseline linear

regression models using these metadata (metadata-only model). Next, we developed deep-learning based models using fundus images (fundus-only model). Lastly, we hypothesized that a model utilizing both types of input data may be even more accurate and thus developed combined models that use both metadata and fundus images (combined model).

First, we compared the performance of metadata-only, fundus-only, and combined models trained to predict Hb, hematocrit (HCT), and red blood cell count (RBC), which are correlated with each other and related to anemia (Fig. 1). The mean absolute error (MAE) for predicting Hb by the metadata-only model was 0.73 (95% confidence interval (CI): 0.72-0.74) g/dL. MAE was 0.67 (95% CI: 0.66-0.68) g/dL for the fundus-only model and 0.63 (95% CI: 0.62-0.64) g/dL for the combined model. The performance of predicting HCT and RBC follow a similar trend across the three models. Thus, the combined model predicted Hb, HCT, and RBC more accurately than either fundus-only or metadata-only models, indicating that both metadata and fundus images are important for the accurate prediction.

Additionally, we investigated whether errors made by the model were patient-specific. In the test set, 342 patients had two visits with both fundus images and a Hb measurement. We applied the combined model to the two visits and found that the residual error was correlated between multiple visits over time by the same patient (Fig. 2, Pearson's correlation coefficient $r = 0.38$ (95% CI: 0.18-0.65)).

Next, we examined if fundus images can be used to predict anemia by developing a DL based classification model to directly predict whether a patient is anemic. Using World Health Organization's (WHO) Hb cutoffs for anemia, we trained the models for three binary classification tasks (anemia, moderate anemia, approximate anemia, see Methods). For all of them, the combined model and the fundus-only model performed better than metadata-only model (Fig. 3, Table 2). The area-under-receiver-operating-characteristic-curve (AUC) for

detecting anemia was 0.73 (95% CI: 0.72-0.75) for the metadata-only model, 0.87 (95% CI: 0.85-0.89) for the fundus-only model, and 0.88 (95% CI: 0.86-0.89) for the combined model (Fig. 3a). AUC for detecting moderate anemia was 0.79 (95% CI: 0.76-0.82) for the metadata-only model, 0.95 (95% CI: 0.93-0.97) for the fundus-only model, and 0.95 (95% CI: 0.93-0.97) for the combined model (Fig. 3b). The sensitivity to detect moderate anemia was 57.3% (95% CI: 47.6-70.5) for the metadata-only model, 91.2% (95% CI: 87.7-94.4) for the fundus-only model, and 92.3% (95% CI: 88.1-95.9) for the combined model, when the specificity was 80% (Table 2). These results show that both the fundus-only model and the combined model successfully extracted information about anemia from fundus images, and it supports the hypothesis that DL model can help detect anemia using fundus images.

We further investigated the importance of different anatomic features to the prediction by “ablating” different aspects of the images during both model training and validation (Fig. 4 and 5). Most notably, when the top and bottom parts of the images were masked, the performance started to decline only after about 80% of each image was masked (Fig. 4a, b). Masking the horizontal stripes through the middle of the images decreased the performance after about 20% of each image was masked (Fig. 4d, e). When either the circular central core or the outer rim of the image was masked, the performance started to decline after about 40% was masked (Fig. 4g, h, j, k). The biggest drop in AUC when 10% of the image was masked occurred while masking the central horizontal stripe: an AUC drop of about 3%. We also examined the effect of Gaussian blurs (Fig. 5), and found that applying a Gaussian blur with $\sigma = 8$ pixels decreased the AUC for predicting moderate anemia from 0.92 to 0.83 (Fig. 5c).

Lastly, we examined if other components of the complete blood count (CBC) could be predicted from fundus images. Anemia is diagnosed based on blood Hb measurements, which is often measured as a part of the CBC. In addition to Hb, HCT, and RBC, other measurements

such as the mean corpuscular volume (MCV) also help to diagnose anemia and identify the subtype. Since the different components of CBC are measured on separate scales, we compared the model's performance across tests with the R^2 coefficient of determination. The combined model was not able to predict MCV with high accuracy, with a low R^2 of 0.12. On the other hand, the model predicted the three anemia-related measurements (Hb, HCT, and RBC) most accurately, R^2 values of 0.52, 0.49, and 0.36, respectively (Table S1).

Discussion

This study shows that a DL-based approach leveraging retinal fundus images and metadata can both detect anemia and quantify Hb measurements, potentially enabling automated anemia screening using fundus images.

To help put the accuracy of our and other non-invasive anemia detection methods in context, it can be useful to consider the variability of the ground truth itself^{25,26}. As consistent with other studies, the ground truth in this study was Hb measured by laboratory hematology analyzers²⁷. The standard deviation of the difference between hematology analyzers and the hemoglobincyanide method (HiCN, the gold standard for Hb measurement for research) was 0.18 g/dL²⁸, equivalent to MAE of 0.14 g/dL. Thus a portion of our model's MAE (0.63 g/dL) may be attributable to variability in the laboratory Hb measurement. The accuracy of our approach is also comparable to invasive (pooled standard deviation of difference was 0.64 g/dL²⁹, equivalent to MAE of 0.51 g/dL) and non-invasive point-of-care devices (pooled standard deviation was 1.4 g/dL^{29,30}, equivalent to MAE of 1.1 g/dL), and non-invasive smartphone-based application (95% limits of agreement was 2.4 g/dL⁹, equivalent to MAE of 0.96 g/dL) (Table 3).

In addition, because fundus photographs are routinely captured as part of teleretinal screening for diabetic retinopathy^{31–33}, the ability to predict Hb from these photographs may provide a convenient way for anemia screening in diabetics with minimal additional cost. The clinical motivation and utility of anemia screening in diabetics is many-fold. First, diabetics can develop chronic kidney disease, which leads to renal anemia³⁴. Second, in patients with diabetic kidney disease, renal anemia often develops earlier than other forms of nephropathy^{35–38}. Even in the absence of nephropathy, Hb in diabetic patients tends to decrease over time^{34,39}. Additionally, the correction of anemia improves the quality of life and may reduce diabetic complications³⁸. Finally, from an ophthalmic standpoint, anemia is an independent risk factor for developing high-risk proliferative diabetic retinopathy⁴⁰. Thus, regular screening for anemia is recommended for diabetic patients^{40–42}.

Beyond the initial diagnosis, subsequent Hb measurements are used to track progression of anemia and response to treatment. In addition, even without a diagnosis of anemia, rapid decrease in Hb may indicate existence or onset of an underlying disease. Thus, in addition to the Hb level at one visit, the difference in Hb across visits is clinically important. Interestingly, our prediction error between multiple visits of the same patient was correlated, showing that some component of the error is patient-specific. When comparing the differences in predictions across multiple visits, the patient-specific components cancel out. Thus, our approach may provide additional value in monitoring the trend in Hb. This premise will be further supported by future work, such as assessing the time delay between true Hb changes and changes in Hb predicted by the algorithm using fundus images: whether the prediction of the model reflects instantaneous Hb or the average Hb over a certain time window. Understanding how the algorithm works would help answer this question. If the algorithm is quantifying the degree of pallor in the fundus, we would expect minimal to no time delays in the order of

minutes or hours. On the other hand, if the algorithm is examining features in microvasculature that develop over time, the time delay may be weeks or months. Investigating how the algorithm reflects recent Hb changes and validating it with multiple measurements over time will be an important step toward determining clinical use cases of the algorithm.

To understand the underlying mechanisms of the model, we examined how the performance was affected by applying image ablation. First, we hypothesized that if the algorithm was based on the degree of pallor of the fundus as a whole, applying a Gaussian blur would have little effect on the performance. However, applying a Gaussian blur decreased the model performance, indicating that the model was dependent on the fine spatial features of the fundus images. In addition, we applied various masking methods to examine which portions of the fundus images are relevant to the model performance. Masking the top and bottom parts had little to no effect on the model performance, showing that the information contained in those areas was redundant. Masking the central core, which includes macula, had less effect than masking the horizontal stripe through the middle part, which includes both macula and disc. These results suggest that fine spatial features around the optic disc are crucial. Future studies could investigate this hypothesis further using multiple explanation techniques.

Another aspect of understanding the algorithm is whether it is detecting anemia or the underlying pathophysiology specific to each subtype of anemia. Anemia has multiple subtypes, and each has a different underlying etiology and requires different management. Other components of the CBC, in particular the MCV (average volume of red blood cells), are used to differentiate between the subtypes. For example, while iron-deficiency anemia typically presents with normal MCV, vitamin B12 or folate deficiency typically presents with elevated MCV, and anemia of chronic disease and thalassemia presents with decreased MCV. Thus, we hypothesized that if fundus images contained information about subtype-specific

pathophysiology, the algorithm would be able to predict CBC results beyond Hb, RBC and HCT. However, the results did not support this hypothesis, indicating that the algorithm may be responding to features associated with the lack of hemoglobin itself. These results also illustrate that the algorithms may be useful for screening, but not for diagnosis. Patients would require referral and follow-up examinations such as blood tests before treatment.

When developing machine-learning-based algorithms, it is crucial to include a broad range of examples in the training set so that the developed algorithm generalize well in various settings. One of the limitations of our study is that we have used a dataset from a single source. For example, ethnicity is highly biased towards Caucasians in the UK Biobank dataset. Training and validating on multiple diverse datasets will be important for creating a generalizable algorithm.

To conclude, we showed that anemia and Hb level can be predicted from fundus images. Further research is warranted to examine if the approach is useful for scalable screening of anemia.

Methods

Study participants

The dataset for this study consisted of fundus images obtained from the UK Biobank²⁴, an observational study that recruited 500,000 participants, aged 40-69, across the United Kingdom between 2006 and 2010. The study was reviewed and approved by the North West Multi-Centre Research Ethics Committee. Each participant was consented and went through a series of health measurements and questionnaires. Each participant also provided blood, urine, and saliva samples. Approximately 70,000 patients also subsequently underwent

ophthalmological examinations with paired retinal fundus and optical coherence tomography (OCT) imaging using a Topcon 3D OCT 1000 Mk2 (Topcon Corporation, Tokyo, Japan). Only retinal fundus images were included in this study. About 12% of the patients were excluded due to poor image quality as described previously²². Only patients with at least one fundus image paired with Hb measurement were included in this study (n=57,163). For complete blood count (CBC) analysis, only the patients who had all the CBC components measured were included (n=53,473). If a patient had multiple visits with paired fundus images and Hb measurement, only the first visit was included, except in the multiple-visit analysis described. The study was reviewed and approved by the North West Multi-Centre Research Ethics Committee. We randomly divided this dataset into a development set to develop our models (80%) and a validation set to assess our model's performance (20%) after stratifying patients by their gender and age. The validation set was not accessed during model development. 10% of the data in the development dataset ("tuning dataset") was used during model development for tuning hyper parameters such as learning rate and criterion for early stopping, with the remaining 70% ("training dataset") used for training the parameters of the neural networks.

Definitions of anemia

Using WHO's guidelines⁴³, we used three sets of cut-offs based on Hb measurements: 12 g/dL for women and 13 g/dL for men (anemia), and 11 g/dL (moderate anemia). In addition, we assessed our results using a previously described gender neutral average anemia cutoff at 12.5 g/dL⁹ for both men and women, which we call "approximate anemia".

Categories of predictive models

In this study, we made two different types of predictions: continuous values (e.g. Hb or hematocrit; henceforth "regression tasks"), categorical values (e.g. presence or absence of

anemia; henceforth “classification tasks”). Though a single model can in principle be trained for both regression tasks and multiple classification tasks, separate models were trained for regression tasks and classification tasks to keep the loss functions on a consistent scale. For each of these tasks, we compared the ability of three different categories of prediction models, each with a different set of input data. As a baseline, we used linear regression for regression tasks and logistic regression for classification tasks. These linear and logistic regression models used only demographic and clinical information (“metadata”, which are ethnicity, age, sex, current smoking status, systolic and diastolic blood pressure, pulse rate, height, weight, and body mass index (BMI)). We will refer to these as “metadata models”. Our second type of models used a deep convolutional neural network (details in the next section) with fundus images as input (“fundus-only models”). Our third and last type of models used both metadata and fundus images as input; the metadata was concatenated with the output of the Inception-v4 architecture⁴⁴ before the fully connected layer (“combined models”). Specifically, the fundus images were used as an input to a deep convolutional neural network (same structure as the fundus-only model), and the output of the convolutional neural network and metadata were provided to the combined model before the final layer (i.e., a “late fusion” model). The fully connected layer of fundus-only models and combined models had one output for each regression task and multiple outputs for each classification task (each output corresponds to each class).

Development of the deep learning algorithms

Fundus images were preprocessed as previously described²³, while the input metadata and continuous output values (e.g. Hb) were standardized to have zero mean and unit variance. Using these data, a deep convolutional neural network with the Inception-v4 architecture⁴⁴ was

developed and trained in TensorFlow⁴⁵. The Inception-v4 network was initialized using parameters from a network pre-trained to classify objects in the ImageNet dataset⁴⁶, and the weights on the auxiliary connections from metadata were randomly initialized. Mean squared error was used as a loss function for regression tasks, and cross entropy was used for classification tasks. The models were trained with mini-batch stochastic gradient descent with momentum⁴⁷ with linear warm up⁴⁸ using Google Tensor Processing Unit (TPU) accelerators⁴⁹ (see supplementary methods). The learning rate was chosen to minimize the error in the tuning dataset. Since our network had a large number of parameters (43 million), to prevent overfitting training was terminated before convergence using early stopping⁵⁰ based on the performance on the tuning dataset. An ensemble of 10 networks⁵¹ was trained on the same development set, and the outputs were averaged to yield the final prediction. For each patient, the final prediction was the average across both eyes.

Evaluating the algorithms

To evaluate the model performance for continuous predictions, we used the mean absolute error (MAE) and R^2 . For binary classification, we used the area under receiver operating characteristic curve (AUC) and sensitivity at various levels of specificity. To obtain 95% confidence intervals for these performance metrics, we used the non-parametric bootstrap procedure with 2,000 samples and reported the 2.5 and 97.5 percentiles.

Ablation analysis

While applying ablation during both training and validation, we trained the fundus-only model for classification tasks and assessed the performance (AUC for predicting anemia and moderate anemia) of the model without ensembling or averaging across eyes. For each ablation

method (e.g. masking 20% of the fundus at the center), 3 networks were trained, and the performance metrics were averaged across 3 networks.

Code availability

The machine-learning models were developed using standard model libraries and scripts in TensorFlow⁴⁵. Custom code was specific to our computing infrastructure and mainly used for data input/output and parallelization across computers.

Data availability

The data that support the findings of this study are available, with restrictions, from UK Biobank²⁴.

References

1. McLean E, Cogswell M, Egli I, Wojdyla D, de Benoist B. Worldwide prevalence of anaemia, WHO Vitamin and Mineral Nutrition Information System, 1993-2005. *Public Health Nutr.* 2008;12(4):444-454.
2. Stevens GA, Finucane MM, De-Regil LM, et al. Global, regional, and national trends in haemoglobin concentration and prevalence of total and severe anaemia in children and pregnant and non-pregnant women for 1995-2011: a systematic analysis of population-representative data. *Lancet Glob Health.* 2013;1(1):e16-25.
3. Stoltzfus RJ. Iron-deficiency anemia: reexamining the nature and magnitude of the public health problem. Summary: implications for research and programs. *J Nutr.* 2001;131(2S-2):697S-700S; discussion 700S-701S.
4. Milman N. Anemia—still a major health problem in many parts of the world! *Ann Hematol.* 2011;90(4):369-377.
5. Smith RE Jr. The clinical and economic burden of anemia. *Am J Manag Care.* 2010;16 Suppl Issues:S59-66.
6. Shah N, Osea EA, Martinez GJ. Accuracy of noninvasive hemoglobin and invasive point-of-care hemoglobin testing compared with a laboratory analyzer. *Int J Lab Hematol.* 2014;36(1):56-61.
7. Kalantri A, Karambelkar M, Joshi R, Kalantri S, Jajoo U. Accuracy and reliability of pallor for detecting anaemia: a hospital-based diagnostic accuracy study. *PLoS One.* 2010;5(1):e8545.
8. Kasper DL, Braunwald E, Hauser S, Longo D, Larry Jameson J, Fauci AS. *Harrison's Principles of Internal Medicine.* McGraw Hill Professional; 2006.
9. Mannino RG, Myers DR, Tyburski EA, et al. Smartphone app for non-invasive detection of anemia using only patient-sourced photos. *Nat Commun.* 2018;9(1):4924.
10. Barker SJ, Badal JJ. The measurement of dyshemoglobins and total hemoglobin by pulse oximetry. *Curr Opin Anaesthesiol.* 2008;21(6):805-810.
11. Pinto M, Barjas-Castro ML, Nascimento S, Falconi MA, Zulli R, Castro V. The new noninvasive occlusion spectroscopy hemoglobin measurement method: a reliable and easy anemia screening test for blood donors. *Transfusion.* 2013;53(4):766-769.
12. Wittenmeier E, Bellosevich S, Mauff S, et al. Comparison of the gold standard of hemoglobin measurement with the clinical standard (BGA) and noninvasive hemoglobin measurement (SpHb) in small children: a prospective diagnostic observational study. *Paediatr Anaesth.* 2015;25(10):1046-1053.
13. Posey WMC. THE OCULAR MANIFESTATIONS OF ANEMIA. *JAMA.* 1897;XXIX(4):169.

14. Aisen ML, Bacon BR, Goodman AM, Chester EM. Retinal Abnormalities Associated With Anemia. *Archives of Ophthalmology*. 1983;101(7):1049-1052.
15. LeCun Y, Bengio Y, Hinton G. Deep learning. *Nature*. 2015;521(7553):436-444.
16. Gulshan V, Peng L, Coram M, et al. Development and Validation of a Deep Learning Algorithm for Detection of Diabetic Retinopathy in Retinal Fundus Photographs. *JAMA*. 2016;316(22):2402-2410.
17. Krause J, Gulshan V, Rahimy E, et al. Grader Variability and the Importance of Reference Standards for Evaluating Machine Learning Models for Diabetic Retinopathy. *Ophthalmology*. 2018;125(8):1264-1272.
18. Ting DSW, Cheung CY-L, Lim G, et al. Development and Validation of a Deep Learning System for Diabetic Retinopathy and Related Eye Diseases Using Retinal Images From Multiethnic Populations With Diabetes. *JAMA*. 2017;318(22):2211-2223.
19. Liu S, Graham SL, Schulz A, et al. A Deep Learning-Based Algorithm Identifies Glaucomatous Discs Using Monoscopic Fundus Photographs. *Ophthalmology Glaucoma*. 2018;1(1):15-22.
20. Christopher M, Belghith A, Bowd C, et al. Performance of Deep Learning Architectures and Transfer Learning for Detecting Glaucomatous Optic Neuropathy in Fundus Photographs. *Sci Rep*. 2018;8(1):16685.
21. Li Z, He Y, Keel S, Meng W, Chang RT, He M. Efficacy of a Deep Learning System for Detecting Glaucomatous Optic Neuropathy Based on Color Fundus Photographs. *Ophthalmology*. 2018;125(8):1199-1206.
22. Varadarajan AV, Poplin R, Blumer K, et al. Deep Learning for Predicting Refractive Error From Retinal Fundus Images. *Invest Ophthalmol Vis Sci*. 2018;59(7):2861-2868.
23. Poplin R, Varadarajan AV, Blumer K, et al. Prediction of cardiovascular risk factors from retinal fundus photographs via deep learning. *Nature Biomedical Engineering*. 2018;2(3):158-164.
24. Sudlow C, Gallacher J, Allen N, et al. UK biobank: an open access resource for identifying the causes of a wide range of complex diseases of middle and old age. *PLoS Med*. 2015;12(3):e1001779.
25. Bland JM, Altman DG. Measuring agreement in method comparison studies. *Statistical Methods in Medical Research*. 1999;8(2):135-160.
26. Barker SJ, Shander A, Ramsay MA. Continuous Noninvasive Hemoglobin Monitoring: A Measured Response to a Critical Review. *Anesth Analg*. 2016;122(2):565-572.
27. UK Biobank Haematology Data Companion Document. <https://biobank.ctsu.ox.ac.uk/crystal/docs/haematology.pdf>.
28. Gehring H, Hornberger C, Dibbelt L, et al. Accuracy of point-of-care-testing (POCT) for

- determining hemoglobin concentrations. *Acta Anaesthesiol Scand*. 2002;46(8):980-986.
29. Hiscock R, Kumar D, Simmons SW. Systematic review and meta-analysis of method comparison studies of Masimo pulse co-oximeters (Radical-7™ or Pronto-7™) and HemoCue® absorption spectrometers (B-Hemoglobin or 201+) with laboratory haemoglobin estimation. *Anaesth Intensive Care*. 2015;43(3):341-350.
 30. Kim S-H, Lilot M, Murphy LS-L, et al. Accuracy of continuous noninvasive hemoglobin monitoring: a systematic review and meta-analysis. *Anesth Analg*. 2014;119(2):332-346.
 31. Tsan GL, Hoban KL, Jun W, Riedel KJ, Pedersen AL, Hayes J. Assessment of diabetic teleretinal imaging program at the Portland Department of Veterans Affairs Medical Center. *J Rehabil Res Dev*. 2015;52(2):193-200.
 32. Conlin PR, Fisch BM, Cavallerano AA, Cavallerano JD, Bursell S-E, Aiello LM. Nonmydriatic teleretinal imaging improves adherence to annual eye examinations in patients with diabetes. *J Rehabil Res Dev*. 2006;43(6):733-740.
 33. Garg S, Jani PD, Kshirsagar AV, King B, Chaum E. Telemedicine and retinal imaging for improving diabetic retinopathy evaluation. *Arch Intern Med*. 2012;172(21):1677-1678.
 34. Mehdi U, Toto RD. Anemia, Diabetes, and Chronic Kidney Disease. *Diabetes Care*. 2009;32(7):1320-1326.
 35. Singh DK, Winocour P, Farrington K. Erythropoietic stress and anemia in diabetes mellitus. *Nat Rev Endocrinol*. 2009;5(4):204-210.
 36. Thomas MC. Anemia in diabetes: marker or mediator of microvascular disease? *Nature Clinical Practice Nephrology*. 2007;3(1):20-30.
 37. Bosman DR, Winkler AS, Marsden JT, Macdougall IC, Watkins PJ. Anemia with erythropoietin deficiency occurs early in diabetic nephropathy. *Diabetes Care*. 2001;24(3):495-499.
 38. Thomas MC, MacIsaac RJ, Tsalamandris C, Power D, Jerums G. Unrecognized anemia in patients with diabetes: a cross-sectional survey. *Diabetes Care*. 2003;26(4):1164-1169.
 39. Craig KJ, Williams JD, Riley SG, et al. Anemia and Diabetes in the Absence of Nephropathy. *Diabetes Care*. 2005;28(5):1118-1123.
 40. Davis MD, Fisher MR, Gangnon RE, et al. Risk factors for high-risk proliferative diabetic retinopathy and severe visual loss: Early Treatment Diabetic Retinopathy Study Report #18. *Invest Ophthalmol Vis Sci*. 1998;39(2):233-252.
 41. Holland DC, Lam M. Predictors of hospitalization and death among pre-dialysis patients: a retrospective cohort study. *Nephrol Dial Transplant*. 2000;15(5):650-658.
 42. Horwich TB, Fonarow GC, Hamilton MA, Robb MacLellan W, Borenstein J. Anemia is associated with worse symptoms, greater impairment in functional capacity and a significant increase in mortality in patients with advanced heart failure. *J Am Coll Cardiol*.

2002;39(11):1780-1786.

43. WHO. Haemoglobin concentrations for the diagnosis of anaemia and assessment of severity. 2011 (WHO/NMH/NHD/MNM/11.1).
44. Szegedy C, Ioffe S, Vanhoucke V, Alemi A. Inception-v4, Inception-ResNet and the Impact of Residual Connections on Learning. <http://arxiv.org/abs/160207261>. February 2016.
45. Martín A, Ashish A, Paul B, et al. TensorFlow: Large-scale machine learning on heterogeneous systems. 2015.
46. Krizhevsky A, Sutskever I, Hinton GE. Imagenet classification with deep convolutional neural networks. In: *Advances in Neural Information Processing Systems*. ; 2012:1097-1105.
47. Sutskever I, Martens J, Dahl G, Hinton G. On the importance of initialization and momentum in deep learning. In: *International Conference on Machine Learning*. ; 2013:1139-1147.
48. Priya G, Piotr D, Ross G, et al. Accurate, Large Minibatch SGD: Training ImageNet in 1 Hour. *arXiv preprint arXiv:170602677*. April 2018.
49. Jouppi NP, Borchers A, Boyle R, et al. In-Datacenter Performance Analysis of a Tensor Processing Unit. In: *Proceedings of the 44th Annual International Symposium on Computer Architecture - ISCA '17*. New York, New York, USA: ACM Press; 2017:1-12.
50. Caruana R, Lawrence S, Giles L. Overfitting in Neural Nets: Backpropagation, Conjugate Gradient, and Early Stopping. In: *Advances in Neural Information Processing Systems 13: Proceedings of the 2000 Conference*. MIT Press; 2001.
51. Opitz D, Maclin R. Popular Ensemble Methods: An Empirical Study. *J Artif Intell Res*. 1999;11:169-198.

Acknowledgements

This research has been conducted using the UK Biobank Resource under Application Number 17643. We thank Dr. Christof Angermueller from Google Research for his engineering contribution, and Drs. Ali Zaidi, Arunachalam Narayanaswamy, Cameron Chen, Jonathan Krause, and Rory Sayres from Google Research for their advice and assistance with reviewing the manuscript.

Author contributions

AM, GSC, LP, DRW, NH, and AVV designed the research. AM, LP, and AVV acquired data from UK Biobank. AM executed research and analyzed the data. AM, YL, and AVV interpreted the results. AM, AH, YL, and NH prepared the manuscript. All authors contributed to manuscript revision and approved the submitted version.

Competing interests

The authors are employees of Google.

Tables and figures

Table 1. Basic characteristics of the development datasets and the validation dataset.

	Development Datasets		Validation Dataset
	Training dataset	Tuning dataset	
Total no. images	80,006	11,457	22,742
No. of patients	40,041	5,734	11,388
Age (years)*	57.9 (50.0-63.7)	58.0 (49.9-63.7)	57.9 (50.0-63.8)
Females (%)	21,944 (54.8%)	3,152 (55.0%)	6,255 (54.9%)
Ethnicity (%)			
Black	468 (1.2%)	74 (1.3%)	145 (1.3%)
Asian	1,330 (3.3%)	192 (3.3%)	404 (3.5%)
White	36,606 (91.4%)	5,247 (91.5%)	10,369 (91.1%)
Other	1,637 (4.1%)	221 (3.9%)	470 (4.1%)
Current Smoker (%)	3,794 (9.5%)	544 (9.5%)	1,120 (9.8%)
Body mass index (kg/m ²)*	26.6 (24.0-29.7)	26.7 (24.1-29.9)	26.6 (24.1-29.7)
Height (cm)*	168 (162-176)	168 (162-176)	168 (162-175)
Weight (kg)*	76.3 (66.2-87.5)	76.7 (66.4-87.6)	76.3 (66.4-87.8)
Heart rate (bpm)*	67.5 (61.0-74.5)	67.5 (60.5-75.0)	67.0 (61.0-74.0)
Systolic blood pressure (mmHg)*	135 (124-148)	135 (124-148)	136 (124-148)
Diastolic blood pressure (mmHg)*	82 (75-88)	82 (75-89)	82 (75-88)
Hemoglobin concentration (g/dL)*	14.3 (13.4-15.2)	14.3 (13.4-15.1)	14.2 (13.4-15.1)
Distribution of Anemia levels			
None	38,628 (96.5%)	5,539 (96.6%)	10,949 (96.1%)
Mild	1,134 (2.8%)	164 (2.9%)	347 (3.0%)
Moderate	267 (0.7%)	31 (0.5%)	90 (0.8%)

Severe	12 (0.0%)	0 (0.0%)	2 (0.0%)
--------	-----------	----------	----------

* results are presented as median (interquartile range). bpm, beats per minute.

Table 2. Sensitivity at various levels of specificity.

	Specificity		
	70%	80%	90%
Anemia			
Metadata-only	63.3% (60.2-66.3)	52.5% (48.6-56.1)	32.0% (23.9-36.4)
Fundus-only	86.0% (83.9-88.4)	78.5% (74.5-82.4)	64.0% (56.6-69.2)
Combined	86.6% (83.8-88.4)	79.4% (75.3-82.9)	65.2% (60.5-71.1)
Moderate anemia			
Metadata-only	78.0% (66.0-80.7)	57.3% (47.6-70.5)	39.7% (25.0-47.8)
Fundus-only	94.8% (92.8-96.8)	91.2% (87.7-94.4)	86.9% (80.8-90.8)
Combined	96.7% (93.0-97.8)	92.3% (88.1-95.9)	84.2% (71.7-91.3)
Approximate anemia			
Metadata-only	73.5% (72.2-75.1)	65.8% (62.9-67.9)	52.9% (50.8-55.2)
Fundus-only	84.8% (82.6-86.9)	76.4% (73.1-79.1)	63.5% (59.2-67.5)
Combined	86.1% (85.0-88.0)	80.9% (78.6-83.1)	69.7% (66.9-73.6)

Sensitivity is presented with 95% confidence intervals.

Bold indicates the highest sensitivity among the models at each condition.

Table 3. Accuracy of different methods to measure hemoglobin concentration.

	Standard deviation of difference	95% Limits of agreement	(Estimated) MAE (*)
Hematology analyzer ²⁸	0.18 g/dL	0.37 g/dL	0.14 g/dL (*)
Invasive point-of-care devices ²⁹	0.64 g/dL	NA	0.51 g/dL (*)
Non-invasive point-of-care devices ^{29,30}	1.4 g/dL	NA	1.1 g/dL (*)
Smartphone-based method ⁹	NA	2.4 g/dL	0.96 g/dL (*)
Our method (combined model)	0.82 g/dL (0.80-0.85)	1.58 g/dL (1.54-1.64)	0.63 g/dL (0.62-0.64)

(*) Mean absolute error (MAE) was estimated assuming that the error has a Gaussian distribution. Hematology analyzer was compared with hemoglobincyanide method. Other methods are compared with hematology analyzer. For the combined model, the results are shown with 95% confidence intervals.

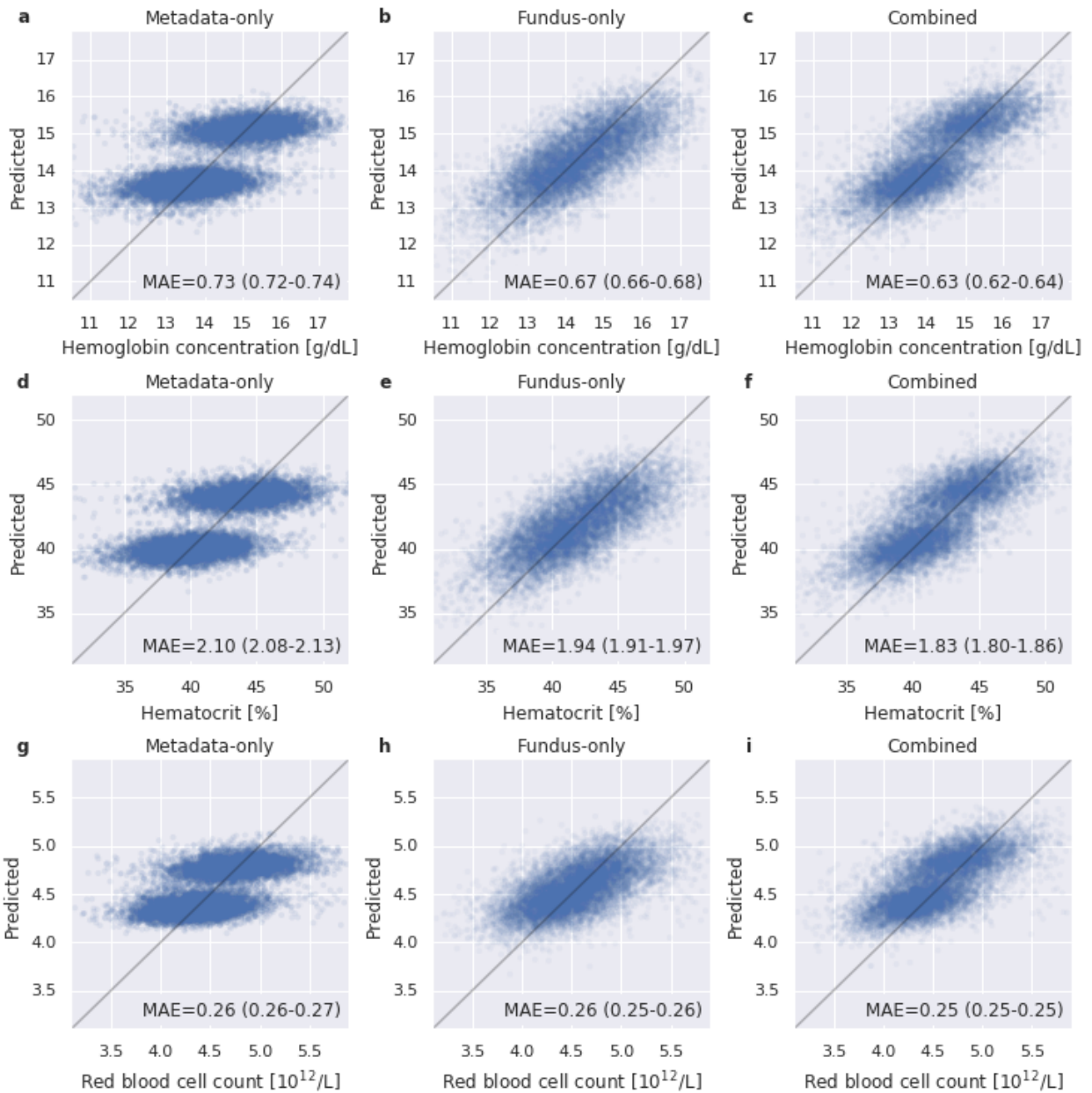


Figure 1. Prediction of hemoglobin concentration, hematocrit and red blood cell count.

a, Each blue dot represents each patient's measured hemoglobin concentration and predicted value from the metadata-only model. Gray line represents an identity line, where measured values equal predicted values. Inset text shows mean absolute error (MAE) with 95% confidence intervals (n=11,388). **b**, same as **a** for the fundus-only model. **c**, same as **a** for the combined model. **d-f**, same as **a-c** for hematocrit. **g-i**, same as **a-c** for red blood cell count.

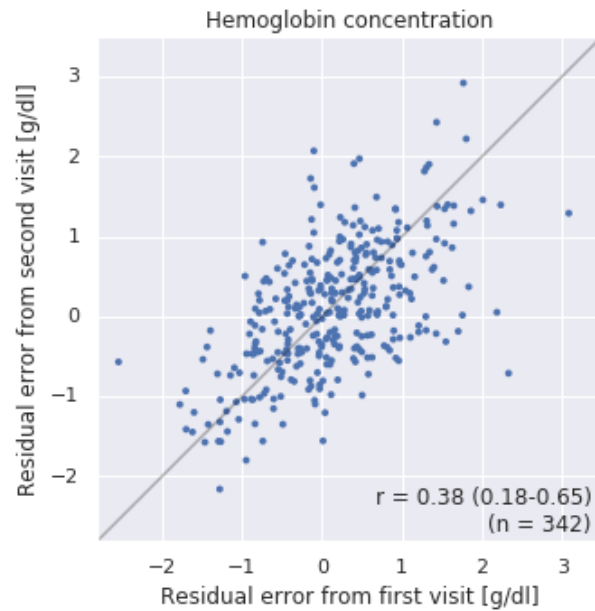


Figure 2. Correlation between residual errors of the combined model from multiple visits.

Each blue dot represents each patient (n=342). Residual error is the difference between measured hemoglobin concentration and prediction by the combined model. Gray line represents an identity line. Pearson's correlation coefficient $r = 0.38$ (95% confidence interval: 0.18-0.65).

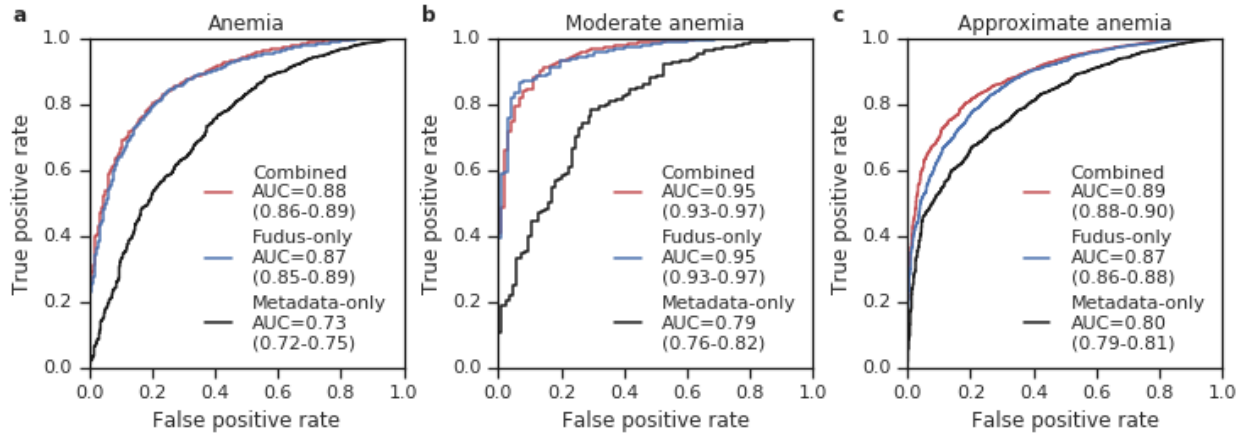


Figure 3. Prediction of anemia classifications.

a, Receiver operating characteristic (ROC) curves for detecting anemia by the metadata-only model (black line), the fundus-only model (blue line), and the combined model (red line). Area under the curve (AUC) for each model is shown with 95% confidence intervals (n=11,388). **b**, ROC curves and AUCs for detecting moderate anemia. **c**, ROC curves and AUCs for detecting approximate anemia (Methods).

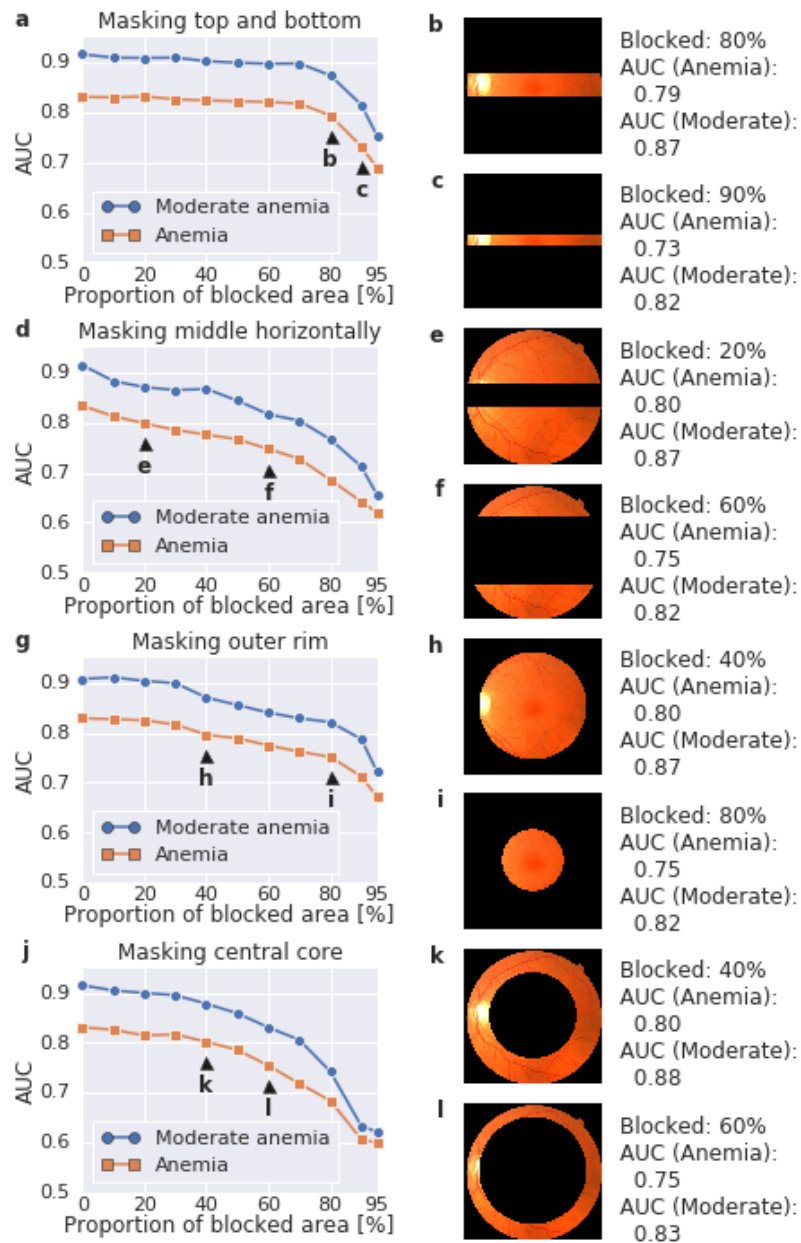


Figure 4. Effects of masking parts of the image on the prediction of anemia and moderate anemia.

The masking was applied during both training and validation. **a**, Masking the top and bottom parts of the images. Arrowheads correspond to examples shown in **b** and **c**. **b** and **c**, Example masked images. **d-f**, Similar to **a-c**, but for masking a horizontal stripe through the middle of the images. **g-i**, Similar to **a-c**, but for masking the outer rim of the images. **j-l**, Similar to **a-c**, but for masking a central core of the images. AUC, area under receiver operating characteristic curve.

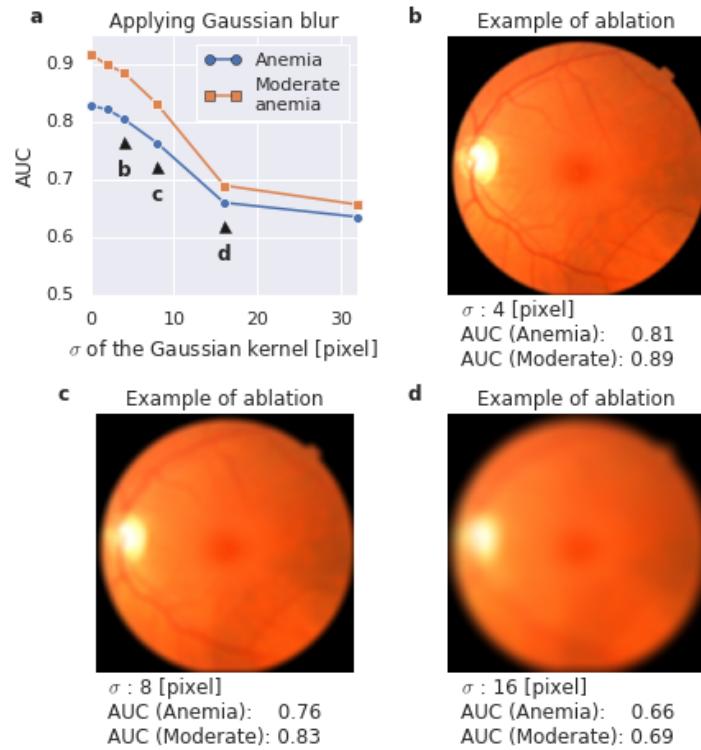


Figure 5. Effects of removing high-frequency information using Gaussian blur on the prediction of anemia and moderate anemia.

The ablation was applied during both training and validation. **a**, Model performance as a function of a Gaussian blur amount. Arrowheads correspond to examples shown in **b-d**. **b-d**, Example images with varying blur amounts. σ , standard deviation of the Gaussian kernel used for a blur, which was applied after images were resized to 587 pixel \times 587 pixel. AUC, area under receiver operating characteristic curve.

Supplementary information

Supplementary methods

We trained each model on a single Google TPUV2 unit (8 cores across 4 chips, 8 GB memory per core, 180 teraFLOPS in total) with the following hyperparameters:

- Inception-v4 architecture
- Input image resolution: 587×587
- Learning rate: 0.0008
 - Learning rate was initially 0.0001, and linearly increased at each step until it reached 0.0008 after 3 epochs⁴⁸.
- Batch size: 64 (8 per core, and 8 cores ran synchronously)
- Batch size for batch normalization: 8 (batch normalization was performed at each core)
- Weight decay: 0.00004
- Mini-batch stochastic gradient descent optimizer with momentum⁴⁷
- Data augmentation (in order):
 - Random vertical and horizontal reflections
 - Random brightness changes with a max delta of 0.1147528
 - Random saturation changes between 0.5597273 and 1.2748845
 - Random hue changes between -0.0251488 and 0.0251488
 - Random contrast changes between 0.9996807 and 1.7704824
- For classification tasks, each class was weighted in proportion to the number of examples of the class to the power of -0.9.
- Model evaluations were performed using a running average of parameters, with an exponential decay factor of 0.9999.

Table S1. Prediction of complete blood count components.

The metadata-only model, the fundus-only model, and the combined model were trained to predict all the complete blood components. Note that the difference from Figure 1 is due to being trained for additional components at the same time and using a smaller subset of patients who had all the components measured. R^2 , coefficient of determination.

Complete blood count components	R^2			Mean absolute error			
	Metadata-only	Fundus-only	Combined	Metadata-only	Fundus-only	Combined	unit
Hemoglobin concentration	0.43 (0.41-0.44)	0.51 (0.50-0.52)	0.52 (0.51-0.53)	0.95 (0.93-0.96)	0.69 (0.68-0.70)	0.67 (0.66-0.68)	g/dL
Hematocrit percentage	0.41 (0.40-0.42)	0.47 (0.46-0.48)	0.49 (0.48-0.50)	2.70 (2.66-2.74)	2.02 (1.99-2.05)	1.96 (1.93-1.99)	%
Red blood cell count	0.32 (0.31-0.33)	0.35 (0.34-0.36)	0.36 (0.34-0.37)	0.34 (0.33-0.34)	0.26 (0.25-0.26)	0.26 (0.25-0.26)	$10^{12}/L$
High light scatter reticulocyte count	0.18 (0.16-0.19)	0.05 (0.04-0.06)	0.18 (0.17-0.20)	0.01 (0.01-0.01)	0.01 (0.01-0.01)	0.01 (0.01-0.01)	$10^{12}/L$
Reticulocyte count	0.16 (0.15-0.17)	0.05 (0.04-0.06)	0.17 (0.15-0.18)	0.02 (0.02-0.02)	0.02 (0.02-0.02)	0.02 (0.02-0.02)	$10^{12}/L$
High light scatter reticulocyte percentage	0.14 (0.13-0.16)	0.03 (0.02-0.04)	0.15 (0.13-0.16)	0.20 (0.19-0.21)	0.15 (0.15-0.16)	0.14 (0.14-0.15)	%
Mean corpuscular hemoglobin	0.11 (0.09-0.12)	0.09 (0.08-0.11)	0.12 (0.11-0.14)	1.79 (1.73-1.85)	1.29 (1.26-1.31)	1.27 (1.24-1.29)	pg
Neutrophil count	0.11 (0.10-0.12)	0.04 (0.03-0.05)	0.12 (0.11-0.13)	1.33 (1.30-1.36)	1.08 (1.06-1.10)	1.00 (0.99-1.02)	$10^9/L$
Immature reticulocyte fraction	0.12 (0.11-0.13)	0.04 (0.03-0.04)	0.12 (0.11-0.13)	0.06 (0.06-0.06)	0.05 (0.05-0.05)	0.04 (0.04-0.05)	ratio
Reticulocyte percentage	0.12 (0.10-0.13)	0.01 (0.00-0.02)	0.12 (0.10-0.13)	0.49 (0.48-0.51)	0.39 (0.38-0.40)	0.37 (0.36-0.38)	%
Mean corpuscular volume	0.11 (0.09-0.12)	0.07 (0.06-0.08)	0.12 (0.10-0.13)	4.35 (4.24-4.47)	3.26 (3.20-3.32)	3.17 (3.11-3.23)	fL
Platelet crit	0.11 (0.10-0.12)	0.07 (0.06-0.08)	0.12 (0.10-0.13)	0.04 (0.04-0.04)	0.03 (0.03-0.03)	0.03 (0.03-0.03)	%
Lymphocyte percentage	0.09 (0.08-0.10)	0.04 (0.02-0.05)	0.09 (0.08-0.10)	7.27 (7.14-7.41)	5.81 (5.72-5.90)	5.64 (5.55-5.73)	%
Platelet count	0.09 (0.08-0.10)	0.04 (0.03-0.05)	0.09 (0.08-0.10)	52.89 (51.86-53.94)	41.34 (40.69-42.00)	40.19 (39.58-40.83)	$10^9/L$
White blood cell count	0.08 (0.04-0.12)	0.03 (0.02-0.05)	0.08 (0.04-0.13)	2.16 (1.71-2.78)	1.41 (1.38-1.44)	1.31 (1.28-1.35)	$10^9/L$
Neutrophil percentage	0.07 (0.06-0.08)	0.02 (0.01-0.03)	0.07 (0.06-0.08)	8.24 (8.09-8.39)	6.56 (6.46-6.66)	6.38 (6.28-6.47)	%
Red blood cell distribution width	0.03 (0.02-0.04)	0.08 (0.07-0.10)	0.07 (0.06-0.08)	0.99 (0.95-1.04)	0.65 (0.64-0.66)	0.64 (0.63-0.65)	%
Mean spheroid cell volume	0.07 (0.06-0.07)	-0.00 (-0.01-0.01)	0.07 (0.06-0.08)	5.10 (4.99-5.21)	4.12 (4.06-4.18)	3.91 (3.84-3.97)	fL
Mean corpuscular hemoglobin concentration	0.05 (0.04-0.06)	0.06 (0.05-0.07)	0.06 (0.05-0.07)	0.79 (0.74-0.85)	0.56 (0.55-0.57)	0.56 (0.55-0.57)	g/dL
Monocyte count	0.06 (0.04-0.07)	0.03 (0.02-0.04)	0.06 (0.04-0.08)	0.20 (0.18-0.22)	0.13 (0.13-0.13)	0.12 (0.12-0.13)	$10^9/L$
Monocyte percentage	0.04 (0.03-0.05)	0.02 (0.01-0.02)	0.04 (0.03-0.06)	2.60 (2.30-2.93)	1.63 (1.60-1.68)	1.59 (1.56-1.63)	%
Platelet distribution width	0.03 (0.02-0.04)	0.02 (0.02-0.03)	0.03 (0.03-0.04)	0.51 (0.50-0.52)	0.40 (0.39-0.41)	0.40 (0.39-0.40)	%
Nucleated red blood cell percentage	0.02 (0.01-0.03)	-0.01 (-0.02-0.00)	0.02 (0.01-0.03)	0.34 (0.27-0.41)	0.05 (0.04-0.06)	0.06 (0.05-0.07)	%
Mean reticulocyte volume	0.02 (0.01-0.03)	0.00 (-0.01-0.01)	0.02 (0.02-0.03)	8.05 (7.87-8.25)	6.21 (6.11-6.32)	6.12 (6.02-6.22)	fL
Nucleated red blood cell count	0.02 (0.01-0.03)	-0.02 (-0.03--0.01)	0.02 (0.01-0.03)	0.02 (0.02-0.03)	0.00 (0.00-0.00)	0.00 (0.00-0.00)	$10^9/L$
Eosinophil count	0.02 (0.01-0.03)	0.01 (0.01-0.02)	0.02 (0.01-0.03)	0.13 (0.12-0.14)	0.09 (0.09-0.09)	0.09 (0.08-0.09)	$10^9/L$
Eosinophil percentage	0.01 (0.01-0.02)	0.00 (0.00-0.01)	0.01 (0.01-0.02)	1.72 (1.65-1.79)	1.22 (1.20-1.25)	1.20 (1.18-1.23)	%
Lymphocyte count	0.02 (0.00-0.07)	0.00 (-0.00-0.02)	0.01 (0.00-0.07)	1.44 (0.72-2.22)	0.52 (0.49-0.55)	0.50 (0.48-0.53)	$10^9/L$
Mean platelet volume	0.01 (0.01-0.02)	0.01 (0.00-0.01)	0.01 (0.01-0.02)	1.08 (1.06-1.10)	0.85 (0.84-0.87)	0.85 (0.83-0.86)	fL
Basophil count	0.01 (0.00-0.01)	0.00 (0.00-0.01)	0.01 (0.01-0.01)	0.05 (0.05-0.06)	0.03 (0.02-0.03)	0.02 (0.02-0.03)	$10^9/L$
Basophil percentage	0.00 (0.00-0.01)	0.00 (0.00-0.00)	0.00 (0.00-0.01)	0.70 (0.61-0.79)	0.34 (0.32-0.35)	0.33 (0.32-0.34)	%